EFFECT OF READER SOFTWARE IN IMAGE QUALITY METRICS OF X-RAY COMPUTED RADIOGRAPHY SYSTEMS

A. Galanopoulou[1], A. Katsigiannis[1], A. Bakas[2], C. Kantsos[2], C. Michail[1], K. Ninos[2], L. Lavdas[2], V. Koukou[1], N. Martini[1], I. Valais[1], G. Fountos[1], I. Kandarakis[1], N. Kalyvas[1*]

[1]Department of Biomedical Engineering, University of West Attica, Egaleo, Greece
[2]Department of Biomedical Sciences, University of West Attica, Egaleo, Greece

Abstract. *X-rays are used in medical imaging to acquire information from inside the human body. The quality of the information is affected by the tube voltage responsible for X-ray penetration and contrast as well as the tube load which affects image noise. Another important part is the X-ray detector. It consists either of a scintillator component coupled to semiconductor (indirect detection) or only of a semiconductor part that directly converts the X-rays to electron-hole pairs which impinge onto an electronic circuit (direct detection). An intermediate solution is the use of a Computed Radiography cassette (CR) which has a scintillator with introduced defaults. These defaults act as traps for the radiation excited electrons and prohibit the spontaneous optical photon generation. The cassette is then excited by a LASER beam provoking the de-excitation of the trapped information carriers. The optical photons generated are collected by a photocathode digitized and presented as an image. The image is further manipulated in an automated manner depending upon the examination. The purpose of this work is to examine the effect of the automated software manipulation to the image quality metrics. A theoretical model based in the linear cascade system theory was utilized. The model has considered the incident X-rays, their absorption in the CR, the generation and trap of electrons, the optical photon generation emission and capture at the photocathode. The model predicted the electrons per incident X-ray as well as the pre-sampled Modulation Transfer Function (MTF) which defines the spatial resolution of the system. The data needed for the model were obtained from literature. The calculation of optical photon transport was done by an analytical solution of Boltzmann diffusion equation. In order to find the effect of the software a PTW edge phantom was irradiated by a BMI GMM X-ray generator and imaged by a FujiFilm ST-VI cassette and a Capsule-X scanner. The images were shown in 'chest', 'patella' and 'PDR' mode to simulate a high latitude, a high contrast and a generic imaging window respectively. The MTF was estimated by Fourier transforming a differentiated edge profile. The contrast was obtained by irradiating the Artinis CDRAD low contrast PMMA phantom and 3Dprinted PLA phantom, both for 'breast' imaging conditions. The data were processed through ImageJ and Octave free software. The best MTF agreement was found for patella imaging conditions. It was found that the image contrast was affected by the phantom material. The PMMA phantom showed better agreement with the experimental results. Since image quality parameters are phantom material based, each new phantom should have a reference image.*

Keywords: *computed radiography, image quality, contrast, modulation transfer function*

1. Introduction

X-rays are utilized in various medical applications like planar imaging, Computed Tomography (CT), dental imaging and interventional radiology [1]. The optimal use of radiation assumes the involvement of high-quality X-ray detectors in the imaging procedure. These image receptors have a high-Z material like Gd, Cs, I, and Ba which enables the efficient radiation absorption through the photoelectric effect. These materials are employed in a chemical form and are doped with an activator, where the energy of the absorbed X-rays is transformed into optical photon energy [2]. Thus, hundreds of secondary information carriers are generated per X-ray photon. By taking into consideration that the digital imaging Si matrix is more sensitive to light than X-rays, the use of these chemical materials, called hereafter scintillators, can reduce the radiation burden of the examination [1]. When the optical photons are captured into the Si matrix they are digitized and bit values are assigned. The resulted image is further processed via image processing software techniques to enhance existing details according to the examination type [1]. One category of X-ray scintillator detectors is the photostimulated phosphors where the X-ray energy absorbed in the material remains trapped in the scintillator by means of electron excitation and detention in lattice defects of the scintillator. The electrons are freed and allowed to return to their basic energy level after a LASER beam excites the material. The electrons de-excitation is followed by the emission of optical photons which propagate in the scintillator, escape and impinge at a photocathode. This type of detection is commonly referred to as Computed Radiography (CR) and the scintillator as photostimulated phosphor (PSP). Although CR is not the state-of-the-art in digital imaging it is currently used as an intermediate solution, because it does not require any modification at the X-ray generator-tube apparatus [1].

The image quality attributes of the final image are usually examined through contrast, that is the ability to detect different tissue types and resolution, that is the ability of discern details. The detector type and image formation process affect the aforementioned parameters. Image quality can be assessed theoretically or experimentally. The theoretical evaluation involves implementation of simulation processes (i.e. Monte Carlo) or the use of Linear Cascaded Systems Theory (LCST) where the stages of image formation from X-ray absorption to pixel creation can be represented by statistical processes. LCST theory has been utilized in the past to determine general mathematical formulas which describe noise and signal transfer in the detector [3]-[9]. In addition, LCST processes have been successfully employed to investigate the image quality metrics of CR systems [10]. Furthermore, image quality is also investigated experimentally by irradiating appropriate X-ray phantoms. The phantom images are used to extract information related to contrast, noise and resolution, either by viewing image details of various sizes, or by calculating the Modulation Transfer Function (MTF) by edge or line images [8], [11]. The scope of this work is to study the effect of the software manipulation to the final image in image quality metrics like MTF and contrast. Towards this end a published theoretical model [10] was used and the parameters describing the statistical stages were theoretically described in order to calculate the MTF. In addition, the MTF of a CR system was measured through the edge method [1], [8] for different built-in imaging appearance software algorithms. Finally, the contrast was experimentally determined by irradiating two contrast detail imaging phantoms [1], [12].

2. MATERIALS AND METHODS

A theoretical model based on the LCST was implemented. LCST theory assumes that image generation can be described by a set of cascaded statistical stages. These are stochastic gain stages and blur stages. In gain stages the signal changes either its initial value (i.e. reduction due to optical photon absorption), or form (i.e. generation of optical photons or electrons per absorbed X-ray photon) [3]-[8]. The gain stages are usually assumed to follow binomial or Poisson distribution [8], [9]. The blur stages are characterized by a dislocation in the signal carrier's position resulting in a Point Spread Function around the point of origin. In spatial frequency domain this is characterized by a corresponding MTF. No signal changes occur in blur stages [3]-[5]. Blur stages may be further subdivided in stochastic blur stages and deterministic blur stages. The latter can effectively describe sampling processes. A more detailed description regarding LCST implementation in scintillator detectors can be found in literature [5]-[7], [10]. The stages of the model considered in this work are shown in Figure 1.

In the first stage, an X-ray spectrum impinge on the CR. The second stage named b considers the X-ray absorption in the material. In this stage it has been assumed exponential X-ray attenuation within the material and subsequent absorption in an elementary layer of thickness t, at depth *j* [5], [8], [9].

The absorbed X-ray photons create electrons that are trapped in the lattice defects. This is presented in the

following stage named c, where the creation of the F-centers [10] has been considered. The F-centers may be partially subject to spontaneous emission. Stage d addresses the LASER excitation and the spatial distribution of the LASER beam. This a blur stage where the spatial distribution of the LASER beam degrades the sharpness of the F-center assumed point of interaction. The degradation can be described in spatial frequency domain by a transfer function, T_{laser}, corresponding to the frequency transform of the LASER power spatial distribution around its center point. Stage e corresponds to LASER movement. The speed in which the LASER moves in order to scan the entire area introduces further unsharpness in the derived image. The unsharpness is directly affected by the scanning speed. This stage can be also characterized by a corresponding transfer function denoted as T_{scan}. The following stage named f, accounts for the LASER de-excitation efficiency.
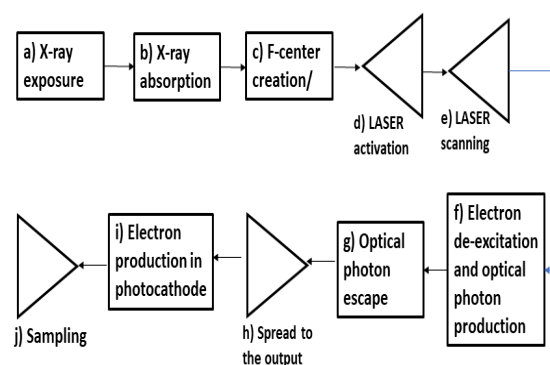

Figure 1. The stages of the theoretical model

In clinical practice the LASER power efficiently provides the required energy for electron de excitation. The probability of electron transition to a lower energy state accompanied with optical photon emission could be as high as 100%. Stage g accounts for the probability of the optical photons generated at depth t to escape to the output. The optical photons, as they propagate, they spread to the output. This is demonstrated in stage h. The spread during propagation is characterized by an additional MTF_{opt} which is a function of the scintillator thickness and optical properties. In stage i the photocathode efficiency as an imaging receptor is consider. This is a gain stage and it is followed directly by a deterministic blur stage, stage j, corresponding to the photocathode spatial sampling and can be described by a related MTF_{pix}. A more detailed description regarding signal processed in a CR system can be found in the work of S. Vedantham [10]. The stages of the model are presented in Figure 1 where the rectangle accounts for gain stages and the triangle for blur stages. Stages a, b, c, f, g and i can predict the total number of electrons, Ne, contributing to the final signal before bit assignment. These can be calculated as:

$$Ne = \sum_E \sum_j f(E)e^{-\mu j} \mu t m_0 E(1-A)P_{FK}G(t)A_{ph}A_{pix} \qquad (1)$$

where *f(E)* is the X-ray energy fluence with energy *E*, *μ* is the X-ray attenuation coefficient, $m_o(1-A)$ is the probability of F-centers creation and remain available for further de-excitation. The value of *A* accounts for the probability of spontaneous emission prior to LASER excitation. *t* is the elementary layer thickness (assumed

5 μm), P_{FK} is the probability of a LASER induced de-excitation, $G(t)$ is the fraction of the optical photons escape to the output, A_{ph} is the photocathode efficiency for producing electrons per optical photon and finally A_{pix} is the pixel size in the final matrix [10].

Stages d, e, h, and j are blur stages which can be characterized by a corresponding Transfer Function in spatial frequency domain. The product of these transfer Functions is the MTF of the system. That is:

$$MTF_{o\lambda} = MTF_{laser} MTF_{opt} MTF_{pix} \qquad (2)$$

where

$$MTF_{laser} = T_{laser} T_{scan} \qquad (3)$$

where T_{laser} was implemented by fitting 2 Gaussian curves in experimental data [10] as:

$$T_{laser}(u) = \frac{1}{2}e^{-0.5u^2} + \frac{1}{2}e^{-0.06u^2} \qquad (4)$$

and

$$T_{scan}(u,\upsilon) = \left|\sin c(\pi\nu_S\tau_D u)\sin c(\pi\nu_{SS}\tau_D\upsilon)\right| \qquad (5)$$

where v is the scanning speed in the scan (subscript s) and the sub-scan (subscript ss) direction. τ_D is the sampling time.

$$MTF_{opt}(u) = \frac{\sum_E \sum_j f(E)e^{-\mu j}\mu t m_0 EG(u,j)}{\sum_E \sum_j f(E)e^{-\mu j}\mu t m_0 EG(0,j)} \qquad (6)$$

The function $G(u,j)$ corresponds to the frequency transform of the optical photons spatial distribution and is a function of the scintillator optical absorption and scatter properties. More details regarding equation (6) can be found in literature [2], [5], [8], [9]. The X-ray spectrum [13], the attenuation coefficients [14], the optical parameters required for the calculation of $G(u,j)$ [5], [8]-[10], the pixel sizes as well as the thickness of the scintillator were obtained from literature. τ_D was set equal to 5 μs, vs=4x10⁴ mm/s and vss=22.6 mm/s [10].

In addition, images of the CDRAD contrast detail phantom accompanied with a similar 3D printed phantom [12] where evaluated in terms of contrast for 'PDR' viewing condition. The material of the CDRAD is PMMA while the corresponding 3D printing phantom was constructed by PLA [12]. In the material of each phantom, holes of different thicknesses have been created. The optical evaluation of the phantom image checks the minimum observable hole thickness. The experimental contrast was evaluated in terms of the pixel value difference between the hole and the background divided by the background pixel value. The contrast was also theoretically determined in terms of subject contrast, by calculating the relative X-ray photon fluence between the phantom material in each hole and the total material thickness, T, divided by the total material thickness.

That is [1] C= [e^{-μ(T-Thole)}-e^{-μT}]/e^{-μT}, where μ is the X-ray attenuation coefficient and T_{hole} is the thickness of the hole in the X-ray propagation direction. The above relationship was summed over the incident X-ray spectrum.

In order to calculate MTF a PTW edge phantom was placed in close contact with a FujiFilm ST-VI cassette having BaClF: Eu⁺ as PSP detector and was irradiated by a BMI GMM X-ray generator [8]. The image was processed in a Capsule-X scanner and the software setup was such that the images to be demonstrated were automatically shown in 'chest', 'patella' and 'PDR' mode. The modes are simulating a high latitude, a high contrast and a generic imaging window respectively. A line profile of the edge image was differentiated and Fourier transformed in order MTF to be calculated. The two low contrast detectability phantoms were exposed to 50 kV X-rays, so as to enhance photoelectric absorption in PLA which is a material of low density. The pixel values of the low contrast phantoms were measured by means of ImageJ software [15].

3. RESULTS AND DISCUSSION

In Figure 2 and Figure 3, a comparison of the calculated MTF for the scan and subscan direction respectively, with literature results [11], for three different types of CR systems is demonstrated. It can be observed that the model produces better results in the scan direction compared to the subscan direction.
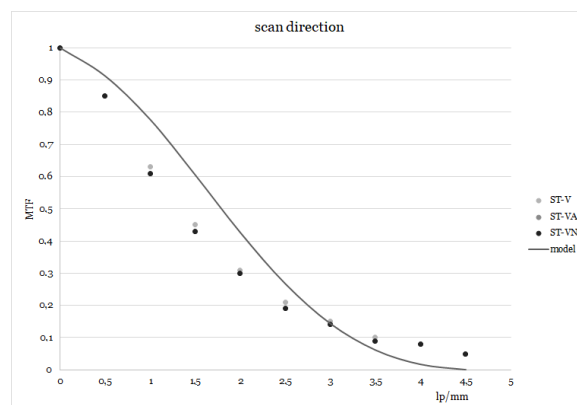

Figure 2. Comparison of theoretical MTF (solid line) with published experimental results obtained by Kengyelics et al [11] for scan direction.
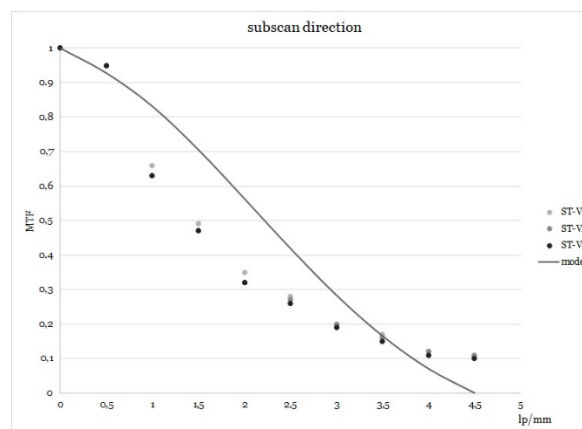

Figure 3. Comparison of theoretical MTF (solid line) with published results obtained by Kengyelics et al. [11] for subscan direction.

In Figure 4, the ESF images as presented by the CR system for 'PDR', 'Chest' and 'Patella' selection are demonstrated. The irradiation was performed at 60 kVp and small focus conditions. It may be observed that the

'Patella' algorithm, optimized for bone imaging retains sharper the edge image. On the contrary the 'chest' option which is optimized for a higher dynamic range, usually presented in a chest X-ray, has enhanced all the pixel values occurred in the signal gradient between the end of the edge and the PSP.
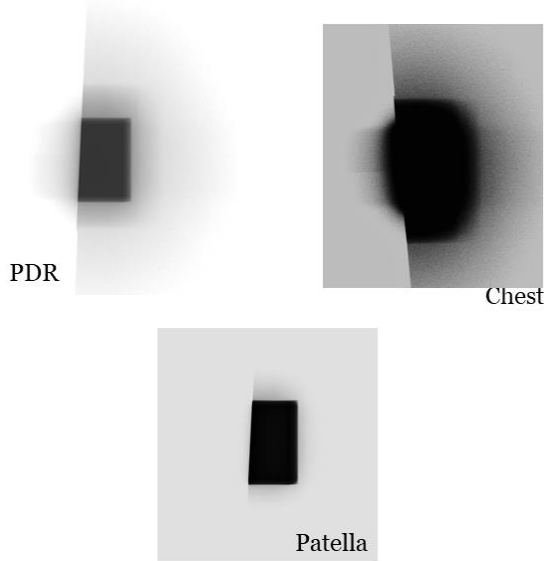

Figure 4. The ESF images for 'PDR', 'Chest' and 'Patella' viewing conditions.
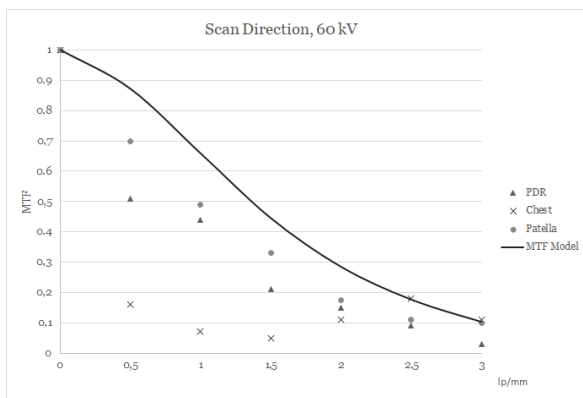

Figure 5. Comparison of theoretical MTF (solid line) with the experimental results corresponding to PDR', 'Chest' and 'Patella'.

In Figure 5, the corresponding experimental MTF curves compared with the theoretical ones for the scan direction are demonstrated. It may be seen that the theoretical values are compared better with the 'Patella' algorithm, since this algorithm retains better the edge characteristics. The deviations between our theoretical MTF and the experimental ones could be attributed to our difficulty in averaging more ESFs in order to obtain less noisy experimental data. Furthermore, the scintillator thickness, the LASER MTF and the photocathode aperture were obtained from literature, thus they may not all correspond to the specific PSP used in the experiments. In addition, the software algorithm imposed to the edge images waved the theoretical and experimental results correlation. When the experimental MTFs are compared it may be seen that the best MTF was that of the 'patella' algorithm,

89

while that of the 'Chest' presented the lowest values per frequency bin. This may be attributed to the fact that the chest X-ray should present a broad dynamic range thus the bit values of the image gradient should be extended. Another reason for the mismatch of the theoretical and the experimental results is that the calculation of MTF with the ESF method requires an edge profile which was difficult to obtain, please see Figure 4. Furthermore the 'patela' algorithm produces steeper images enabling the visualization of abrupt signal changes. This function may be useful in clinical situations where a possible diagnosis of a bone fracture is investigated.

In Figure 6, the image of the CDRAD and the 3D printer PLA constructed phantom is presented for 50 kV exposure conditions. In addition, in Figure 7 and Figure 8 the theoretical and experimental contrast is demonstrated for PLA and PMMA material. As both the phantom images were acquired simultaneously it appears that the CR software visualized better PMMA, which is a material with higher density, than PLA. In every case if a phantom is used for contrast evaluation of a CR detector a reference images should be taken upon systems installation.
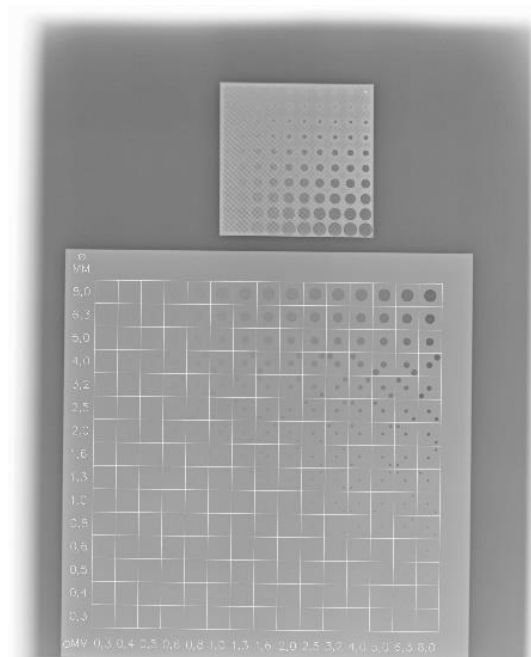

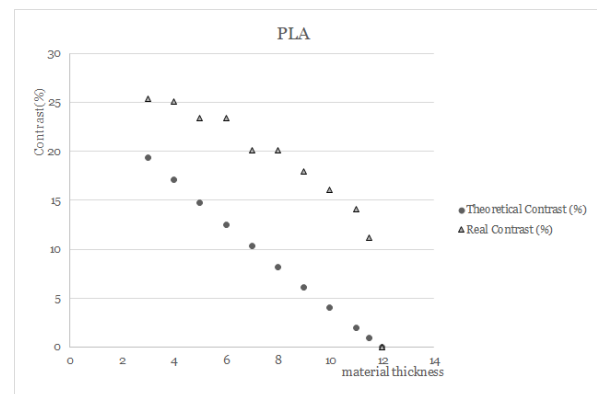Figure 6. Images of the 3D printed (top) and the CDRAD (bottom) phantoms.

Figure 7. Comparison of calculated and measured contrast for the 3D printed phantoms made of PLA.
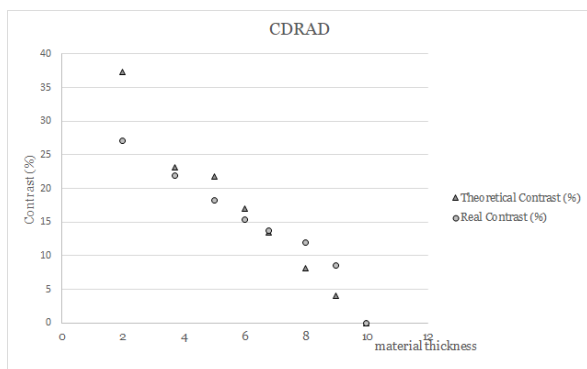
Figure 8. Comparison of calculated and measured contrast for the CDRAD phantoms made of PMMA.

4. CONCLUSION

We have studied the effect of CR software viewing options in terms of MTF and contrast. Towards it, a theoretical MTF model was used and the corresponding MTF results were compared to experimentally determined MTF curves. It was found that high contrast viewing conditions (i.e, skeletal imaging) demonstrates higher MTF values closer to the theoretical ones. Furthermore, two low contrast detectability phantoms were imaged with a 50 kV incident X-ray spectrum. A phantom for image quality assessment can be used in CR systems assuming that a reference image for every available viewing option exists.

REFERENCES

1. H. Aichinger, J. Dierker, S. Joite-Barfuß, M. Säbel, "Principles of X-Ray Imaging," in *Radiation Exposure and Image Quality in X-ray Diagnostic Radiology: Physical Principles and Clinical Applications*, 2nd ed., Berlin Heidelberg, Germany: Springer-Verlag, 2012, ch. 1, pp. 3 – 7.
   DOI: 10.1007/978-3-642-11241-6_1
2. I. S. Kandarakis, "Luminescence in medical image science," *J. Lumin.*, vol. 169, part B, pp. 553 – 558, Jan. 2016.
   DOI: 10.1016/j.jlumin.2014.11.009
3. M. Rabbani, R. Shaw, R. Van Metter, "Detective quantum efficiency of imaging systems with amplifying and scattering mechanisms," *J. Opt. Soc. Am. A*, vol. 4, no. 5, pp. 895 – 901, May 1987.
   DOI: 10.1364/josaa.4.000895
   PMid: 3598742
4. M. Rabbani, R. Van Metter, "Analysis of signal and noise propagation for several imaging mechanisms," *J. Opt. Soc. Am. A*, vol. 6, no. 8, pp. 1156 – 1164, Aug. 1989.
   DOI: 10.1364/JOSAA.6.001156
5. R. M. Nishikawa, M. J. Yaffe, "Model of the spatial-frequency-dependent detective quantum efficiency of phosphor screens," *Med. Phys.*, vol. 17, no. 5, pp. 894 – 904, Sep. 1990.
   DOI: 10.1118/1.596583
6. I. A. Cunnigham, M. S. Westmore, A. Fenster, "A spatial-frequency dependent quantum accounting diagram and detective quantum efficiency model of signal and noise propagation in cascaded imaging systems," *Med. Phys.*, vol. 21, no. 3, pp. 417 – 427, Mar. 1994.
   DOI: 10.1118/1.597401
7. H. K. Kim, S. M. Yun, J. S. Ko, G. Cho, T. Graeve, "Cascaded modeling of pixelated scintillator detectors for x-ray imaging," *IEEE Trans. Nucl. Sci.*, vol. 55, no. 3, pp. 1357 – 1366, Jun. 2008.
   DOI: 10.1109/TNS.2008.919260
8. C. M. Michail et al., "Experimental and theoretical evaluation of a high resolution CMOS based detector under x-ray imaging conditions," *IEEE Trans. Nucl. Sci.*, vol. 58, no. 1, pp. 314 – 322, Feb. 2011.
   DOI: 10.1109/TNS.2010.2094206
9. P. Liaparinos, N. Kalyvas, I. Kandarakis, D. Cavouras, "Analysis of the imaging performance in indirect digital mammography detectors by linear systems and signal detection models," *Nucl. Instrum. Methods Phys. Res. B*, vol. 697, pp. 87 – 98, Jan. 2013.
   DOI: 10.1016/j.nima.2012.08.014
10. S. Vedantham, A. Karellas, "Modeling the performance characteristics of computed radiography (CR) systems," *IEEE Trans. Med. Imaging*, vol. 29, no. 3, pp. 790 – 806, Mar. 2010.
    DOI: 10.1109/TMI.2009.2036995
    PMid: 20199915
    PMCid: PMC5228607
11. S. M. Kengyelics, J. H. Launders, A. R. Cowen, "Physical imaging performance of a compact computed radiograpghy acquisition device," *Med. Phys.*, vol. 25, no. 3, pp. 354 – 360, Mar. 1998.
    DOI: 10.1118/1.598212
12. I. Kapetanakis, G. Fountos, C. Michail, I. Valais, N. Kalyvas, "3D printing x-ray quality control phantoms. A low contrast paradigm," *J. Phys.: Conf. Ser.*, vol. 931, 012026, 2017.
    DOI: 10.1088/1742-6596/931/1/012026
13. *Simulation of X-ray spectra, on-line tool for the simulation of x-ray spectra*, Siemens Healthineers, Erlangen, Germany.
    Retrieved from:
    https://www.oem-products.siemens-healthineers.com/x-ray-spectra-simulation
    Retrieved on: Mar. 15, 2019
14. R. Nowotny, *XMuDat: Photon attenuation data on PC version 1.0.1*, IAEA Nuclear Data Section, Vienna, Austria, 1998.
    Retrieved from:
    https://www-nds.iaea.org/publications/iaea-nds/iaea-nds-0195.htm
    Retrieved on: Mar. 15, 2019
15. W. Rasband, *ImageJ version 1.47h*, National Institutes of Health, Bethesda (MD), USA, 2012.
    Retrieved from:
    https://imagej.nih.gov/ij/
    Retrieved on: Mar. 15, 2019